

Anticipating hyperthermia efficiency of magnetic colloids by a semi-empirical model: a tool to help medical decisions.

M. B. Fernández van Raap^{*a}, D. F. Coral^a, S. Yu^b, G.A. Muñoz^a, F. H. Sánchez^a, A. Roig^b

^aInstituto de Física La Plata (IFLP- CONICET), Departamento de Física, Facultad de Ciencias Exactas, Universidad Nacional de La Plata (UNLP), c.c. 67, 1900 La Plata, Argentina. Tel +54 221 4246062 x 257 Fax +54 221 4236335

^bInstitut de Ciència de Materials de Barcelona (ICMAB-CSIC), Campus UAB, 08193 Bellaterra, Catalonia, Spain

* **Corresponding Author e-mail:** raap@fisica.unlp.edu.ar

Magnetic hyperthermia, a modality that uses radio frequency heating assisted with single-domain magnetic nanoparticles, is becoming established as a powerful oncological therapy. Much improvement in nanomaterials development, to enhance their heating efficiency by tuning the magnetic colloids properties, has been achieved. However, methodological standardization to accurately and univocally determine the colloids properties required to numerically reproduce specific heating efficiency using analytical expressions still holds. Thus, anticipating the hyperthermic performances of magnetic colloids entails high complexity due to polydispersity, aggregation and dipolar interaction always present in real materials to a more or lesser degree. Here, by numerically simulating experimental results and using real biomedical aqueous colloids, we analyse and compared several approaches to reproduce experimental specific absorption rate values. Then, we show that relaxation time, determined using a representative mean activation energy consistently derived from four independent

experiments accurately reproduces experimental heating efficiencies. Moreover, the so-derived relaxation time can be used to extrapolate the heating performance of the magnetic nanoparticles to other field conditions within the framework of the linear response theory. We thus present a practical tool that may truly aid the design of medical decisions.

1. Introduction

Magnetic Hyperthermia (MH) is an oncologic therapy¹ under clinical trials that is achieved by subjecting biocompatible magnetic nanoparticles to external radio frequency fields of 100 kHz and 15 kA/m. Besides that, the synergistic potential of MH combined with other clinically approved treatments like chemo², radio¹ and photodynamic³ therapies is under scrutiny. Iron oxide nanoparticles (IONPs), magnetite (Fe_3O_4) or maghemite ($\gamma\text{-Fe}_2\text{O}_3$), coated with polyprotic acids like dimercaptosuccinic⁴ or citric⁵, polysaccharides like dextran^{6,7} and aminosilane hydrophilic⁸ molecules and well dispersed in water at physiological pH are widely accepted as the most biocompatible materials for MH treatments. For clinical trials of MH associated with radiotherapy, IONPs coated with aminosilane are used¹, Jordan showed that aminosilane coated IONPs displayed better efficiency compared with carboxidextran coated particles⁸.

By rising the temperature, hyperthermia causes living cells death when temperature reaches values in the range from 42 to 46 °C. This abnormally high temperature alters the function of many structural and enzymatic proteins within cells, which in turn alters cell growth and differentiation and can induce apoptosis. Among the various hyperthermia modalities, MH provides spatial selectivity avoiding normal tissue damage. A comparison of the various hyperthermia therapeutic modalities in terms of

clinical results, side effects, limitations can be found in P. Moroz *et al.* review⁹. A more recent review on the status of MH in clinical trials can be found elsewhere¹⁰.

Under the effect on an alternating current (a.c.) magnetic field in the radio frequency range, an assembly of single-domain (SD) magnetic nanoparticles (MNPs) absorbs energy from the field achieving a magnetization which lags in phase relative to the excitation wave¹¹. The energy absorbed by the nanoparticles is then released to its environment. When the MNPs located in tumour tissue are subjected to the a.c. field and release enough energy to increase the temperature up to therapeutic values (42 - 45 °C), the apoptosis of tumour cancer cells is induced¹². Temperature increase above 45 °C and up to 50 °C results in cell/tumour ablation. Results presented here are useful for both hyperthermia and ablation. A parameter often used to characterize the MNPs efficiency at a given field is the specific absorption rate (SAR), keeping in mind that this parameter depends on field condition.

In addition, RF heating has also been proposed in drug delivery application. Nanoparticles are designed to release their drug payload in response to an external stimulus like light, ultrasound, heat and medium acidity¹³. Iron oxide nanoparticles embedded in poly(lactic-co-glycolic acid) and loaded with paclitaxel have been recently reported where magnetic hyperthermia was used to trigger drug release by Néel relaxation¹⁴. Interestingly authors were able to correlate the SAR values of the investigated systems with the particle size obtained from the ¹H nuclear magnetic resonance dispersion profiles and argued that proton nuclear magnetic resonance could be used to predict SAR of new systems.

Regarding medical aspects, Hilger¹⁵ has stressed in her recent *in-vivo* review that besides the huge advantage coming from the fact that heating is generated within the tumour and not from outside the body, the optimal dose of MNPs and their intratumoral

distribution are key factors determining the therapeutic outcome. In addition, dosage relies on nanoparticle properties and on administration routes. It was early recognized that the optimization of the nanoparticles properties will allow reducing the dose and the use of moderate a.c. fields in terms of field frequency, f , and field amplitude, H_0 (within biomedical safe range of a.c. applications i.e. $f \cdot H_0$ below $4.85 \times 10^8 \text{ Am}^{-1} \text{ s}^{-1}$) to achieve the desired effect. To this end, it is essential to enhance heating efficiency of iron oxide nanoparticles¹⁶, reduce early clearance from the body and minimize non-specific cell interactions, thus minimizing side effects. This situation has led to the improvement of chemical synthesis and coating protocols for producing IONPs sterically or electrostatically stabilized in physiological medium and to provide specificity for intravenous applications. These protocols include co-precipitation of iron salts^{17,18}, thermal decomposition of metal complex^{19,20}, hydrothermal polyol process²¹ and laser target evaporation²² among others. More recently, these methods have been enlarged by improving heating during chemical reactions with the assistance of microwaves (MW)^{23,54}. MW-assisted routes display the advantages of producing particles in high yields within few minutes and that the particles are straightforwardly stabilized as aqueous colloidal dispersions at physiological pH. This avoids the ligand exchange step needed in conventional thermal decomposition route which often results on partial aggregation of the particles. Using microwave-based method, the synthesis of water stable citric-acid coated multi-core iron oxide nanoparticles suitable for magnetic heating has been reported²⁴.

Besides magnetosomes, which may not be suitable for biomedical applications unless prepared in specific conditions²⁵, the largest specific heating efficiencies have been reported for crystalline magnetite nanoparticles with core sizes between 20 and 30 nm, in the transition zone between single magnetic domain and multidomain²⁶, values as

large as $300 \text{ W/g}_{\text{Fe}}$ for 22 nm at 77 kHz and $40 \text{ kA}\cdot\text{m}^{-1}$ were achieved. Spherical clusters (60 nm size) of carboxymethyl dextran coated iron oxide nanoparticles of 18 nm dissipate 720 W g^{-1} when excited at 10 kA m^{-1} and 410 kHz¹⁸ and nanoflower like assemblies²¹ dissipate $1175 \text{ W}\cdot\text{g}^{-1}$ when excited at $21.5 \text{ kA}\cdot\text{m}^{-1}$ and 700 kHz. Cubic shape particles also display large SAR values due to shape anisotropy contribution²⁷. SAR values of several nanoparticles under excitation frequencies larger than 200 kHz in various environments have also been recently reported²⁸. Another way to improve the SAR is by modifying MNP chemical composition, for instance by doping with Zn⁴⁶ or Mn to increase magnetization that effectively leads to an increase in the MNPs heating efficiency, or by using exchange coupled nanomagnets, combining hard and soft magnetic phases like $\text{CoFe}_2\text{O}_4@\text{MnFe}_2\text{O}_4$ ²⁹. In all of these studies SAR trends are verified but measured SAR magnitudes were not theoretically reproduced.

Moreover, nanoparticles aggregation influences the heat dissipation, and contradictory results have been reported. A negative influence of aggregation on SAR has been observed in samples where the aggregates are composed of randomly oriented spherical nanoparticle^{30, 31, 32}. Matera *et al.*³³ have analyzed the performance of mesoscale assemblies of cubic IONP to generate control aggregation. The authors showed that the hyperthermia performance of those aggregates was lower than that of their counterpart IONPs due to dipolar interactions. On the other hand, it has been proposed that assembling cubic particle in elongated chains (uniaxial anisotropy) is a strategy to increase the MH performance^{27,34}. Furthermore, the possibility of controlling heating power by tuning dipolar interactions first led to controversial results indicating both increasing and decreasing SAR with increasing concentration^{20,35,36,37,38}. We have recently clarified this point by proving experimentally that the power dissipated by an ensemble of monodisperse magnetic nanoparticles becomes a non-extensive property as

a direct consequence of the long-range nature of dipolar interaction, i.e. specific heat dissipation displays a maximum against concentration³¹. Similarly non-monotonic concentration dependence was shown by Conde-Leboran *et al.*³⁹. This concentration trend had been already proposed by Landi^{40, 41} using a random dipolar-field approximation, for mean first order fluctuating dipolar field contribution averaging to zero, i.e. only valid for an ensemble of monodisperse MNPs. Hase *et al.*⁴² based on the Landau-Lifschitz-Gilbert equation of motion solved with Langevin dynamics for various spatial distributions of the MNPs indicated negative influence of the dipole-dipole interactions on heating power and a maximum in the heating power per sample volume *vs* concentration. In spite of these efforts, the only parameters that nowadays can be used to control heating are the field parameters f and H_0 but to this end a way to predict SAR magnitude of a given colloidal system has to be established. Abenojar *et al.* have recently published a more detailed review including size, shape, chemical composition and dipolar interactions effects on magnetic hyperthermia and more importantly, have introduced a new theranostic modality based on magnetic imaging guided-hyperthermia⁴³.

In general, a fingerprint of highly dissipating MNP assemblies is a blocking temperature (T_b) close or above room temperature, for an experimental temporal window, typical of d.c. magnetometry. For instance, a progressive shift of T_{bm} (the maximum shown by zero-field-cooled magnetization) from 70 K to temperatures higher than 300 K was observed by Salas *et al.*⁴⁴ on highly crystalline, monodisperse, and interactive assemblies of SD-IONPs coated with meso-2,3-dimercaptosuccinic acid, when the MNPs size increased from 7 to 22 nm (SAR increase from 4.62 to 320 W/g_{Fe}). Di Corato *et al.*²⁸ reported T_{bm} going from 135 K to values larger than 320 K for samples going from co-precipitated maghemite nanoparticles ~ 10 nm size (135 K), to a 250 nm

assembly of the same maghemite nanoparticles in liposomes (165 K), iron oxide/gold dimers 15 nm (175 K), iron oxide nanoflowers 25 nm (280 K), iron oxide nanocubes of 18 nm on edge (300 K) and cobalt ferrite nanoparticles of 10 nm size ($\gg 320$ K), together with increasing SAR magnitudes. The blocking temperature increase with MNP size and the value corresponding to a given size shift to higher values when dipolar interaction strength increases⁴⁵. Unfortunately, T_{bm} for these highly dissipating colloids is above the limit of the available temperature range of standard SQUID and PPMS magnetometry measuring systems.

Although, much knowledge has been established there is still no clear consensus about the specific key features of a colloid needed for predicting its SAR. Nor about the analytical expression to semi-empirically reproduce measured SAR values. Exhaustive structural and magnetic characterizations of the so-produced colloids are commonly carried out to derive interrelation between nanoparticle physical properties and their specific heating efficiency, but these properties are barely use to numerically reproduced experimental SAR values. Attempts to numerically reproduced measured SAR magnitudes^{31,46,47,48,49,50} in general failed because the MNPs dispersions present polydispersity, aggregation and dipolar interaction and there is a lack of knowledge about the effect of these properties on the energy barrier and relaxation time. Also discrepancies between characteristic magnitudes derived from different techniques appear. In this sense standardization of the measurement protocols to accurately and univocally determine colloids properties is still needed. For instance, there is often discrepancies between effective anisotropy constant K_{eff} values derived by d.c. and a.c. magnetometry, as well as a diversity of criteria to retrieve this magnitude from raw data and Néel prefactor τ_0 , values in a range as wide as 10^{-12} - 10^{-8} s are used. Then, which are the physical properties of a given suspension on MNPs that must be determine, and how,

to securely predict its heating efficiency at any pre-set applied field using an analytical expression is still an open question. This is indeed the main goal of this work since it would constitute a practical tool to assist medical decisions. More precisely, to decide which is the optimal dosage of a given nanoparticle to be intra-tumorally injected considering the tumour volume in order to achieve the desired temperature increase, ΔT , in a time t under excitation of parameters f and H_0 .

To this end, we tested the applicability of quasi-static (d.c.) and low frequency a.c. methodologies to derive the activation energy which defines Néel relaxation times, and to numerically reproduce experimentally measured SAR data. We have analysed five model systems of stable colloidal aqueous suspensions holding: citric acid coated γ - Fe_2O_3 nanoparticles produced by a microwave-assisted thermal decomposition method⁵³, two different multicore suspensions of chitosan particles holding aggregated Fe_3O_4 nanoparticles or holding well dispersed MNPs prepared by co-precipitation of magnetite followed by chitosan nanoprecipitation on as-formed MNP⁵¹ and uncoated Fe_3O_4 prepared by conventional co-precipitation protocol⁵². With these assemblies of SD-MNPs a range of mean sizes from 5 to 14 nm is covered. These suspensions display distinctive interparticle interaction strength and different degree of MNP size polydispersity and aggregation. In spite that, these colloids are not highly dissipative and they were selected because, with the exception of the uncoated MNPs, their blocking temperatures (for d.c. magnetometry measuring time $\tau_m \sim 100$ s) are below room temperature. In highly diluted colloids of single particles, the MNPs are almost non-interacting this constitute an easier study case but far from useful in a therapeutically scenario since by lowering the concentration larger amounts of suspension, out of tumour capacity, would have to be injected to achieve the desired temperature. Magnetocalorimetric measurement, a.c. and d.c. magnetometry were used

to determine mean activation energy, and to confirm the presence of interparticle interaction. Transmission electron microscopy (TEM) and cryo-TEM were used to determine mean nanoparticles size, and its dispersity and the occurrence of aggregation. The so-derived physical properties were used to numerically simulate SAR and to validate the extrapolation to other field conditions.

2. Experimental Section

2.1 Synthesis of SD-IONPs suspensions.

In this work five colloidal aqueous suspensions are analysed. Two were obtained using microwave (MW)-assisted thermal decomposition method at 180 °C and 210 °C followed by electrostatic stabilization with tri-sodium citrate (Na₃Cit). These samples consist of γ -Fe₂O₃ particles of mean magnetic core size of 5.6 and 8.0 nm and are labelled as Cit/MNP-6 and Cit/MNP-8. Other two samples were produced by coprecipitation of iron (II) sulfate and iron(III) chloride hexahydrate with the addition of oleic acid (OA) to produce coated Fe₃O₄ nanoparticles followed by a second step where these particles were coated with chitosan (CS). The mean magnetic core sizes of these particles are 5 and 10 nm, and are named here as CS/MNP-5 and CS/MNP-10. This material consists of large CS particles holding well-spaced MNP particles in the former case and quite aggregated particles in the later. A deeper discussion on synthesis protocol and physicochemical characterization as well as magnetic characterization can be found elsewhere^{51,47}. Finally, a colloid of uncoated magnetite, named here U/MNP-14, was used. These particles of mean size around 14 nm were produced by coprecipitation of iron(III) chloride hexahydrate and iron(II) chloride tetrahydrate. Synthesis details and a complete structural and magnetic characterization have been previously published⁵². The main structural characteristics are schematized in figure 1. MW-assisted thermal decomposition method was used to synthesize pristine SD-IONPs

in a CEM Discover reactor (Explorer 12-Hybrid) at a frequency of 2.45 GHz and 300 W. Synthesis process is described in Yu *et al.*⁵³ following a slight modification from Pascu *et al.*⁵⁴. Briefly, 0.124 g (0.35 mmol) of tri-(acetylacetonate) iron(III) ($\text{Fe}(\text{acac})_3$) were dissolved completely in 4.5 mL anhydrous benzyl alcohol in a special MW-tube and vortexed for 30 seconds. Reaction tubes were transferred to the microwave reactor, the heating ramps were 5 min at 60 °C and 10 min at 180 °C or 10 min at 210 °C for the 5.6 and 8.0 nm particles respectively. Once the reaction finished, 150 μL 10 wt.% Na_3Cit were added to each MW-tube and sonicated during 1min. Then, the suspension of SD-IONPs in each tube was divided into 2 equal parts in separate 50 mL centrifugal tubes. Each centrifugal tube was filled up to 50 mL with acetone and subjected to centrifugation at 6000 rpm for 30 min. The supernatant was discarded and the operation was repeated twice. SD-IONPs were washed and centrifuged again at the same conditions. Collected SD-IONPs pellets were dried overnight in oven at 60 °C and dispersed in 2 mL MilliQ water. Colloid concentration $[X]$ was determined by flame atomic absorption spectroscopy using a Perkin-Elmer spectrometer. To obtain CS/MAG nanoparticles, 3.27 g of $\text{FeCl}_3 \cdot 6\text{H}_2\text{O}$ (12.1 mmol of Fe^{3+}) and 0.981 g of FeSO_4 (6.46×10^{-3} mol Fe^{2+}) were dissolved in 100 mL of distilled water and OA was incorporated to the mixture. Then, 25 ml of NaOH 5M were added at controlled rate to precipitate the oxide. The mixture was allowed to complete the magnetite formation during 30 min. Washing cycles with bi-distilled water were carried out three times. The solid was dried at 45 °C overnight under vacuum. In a second step, 450 mg of CS was used to hydrophilize, 300 mg of oleic-acid coated magnetite (OA/MAG) nanoparticles (2/3 of CS to OA/MAG w/w) previously synthesized with different mass ratio of oleic acid to magnetite (1/1 and 4/1). Around 300 mg of OA/MAG were dispersed in acetone under sonication during 15 min. Then, the adequate volume of a solution of 9.73 mg/ml

of CS in acetic acid (50%) was incorporated. The solid nanoparticles decanted immediately. The supernatant was removed and the solid re dispersed in distilled water. For uncoated magnetite, 2.75 g of $\text{FeCl}_3 \cdot 6\text{H}_2\text{O}$ (10.2 mmol of Fe^{3+}) and 1.01 g of $\text{FeCl}_2 \cdot 4\text{H}_2\text{O}$ (5.1 mmol of Fe^{2+}) were dissolved in 50 mL of bi-distilled water each, mixed and heated to 60 °C. Then, 3 mL of NH_4OH solution (25% w/w) was added drop by drop and left to react for 30 min; after that, 75 mL of ammonia solution were added until the solution reached a pH of 10.5. Then, the black precipitate was separated from the dispersion medium, washed several times and re-suspended in water at a pH = 7.

2.2 Structural and magnetic characterization

TEM micrographs and electron diffraction (ED) images were obtained with a JEOL JEM-1210 electron microscope, operating at 120 kV. The mean diameter and polydispersity of each system were determined by counting and sizing over 300 particles from TEM images using ImageJ software and fitting a Gaussian distribution to the resulting particle size histograms. Samples for cryo-transmission electron microscopy (cryo-TEM) were prepared as follows: 3 μL of 2.5 $\mu\text{g}/\text{mL}$ IONPs were placed onto a Quantifoil® grid where a perforated foil was used to bear an ultra-thin carbon support foil to minimize the total specimen thickness. The drop was blotted with filter paper and the grid was quenched rapidly into liquid ethane to produce vitreous ice, avoiding the formation of crystals. The grid was then transferred into the TEM microscope (JEM-2011 operating at 200 kV), where the temperature was kept at 133 K by the use of liquid nitrogen during the imaging.

The hydrodynamic sizes of the nanoparticles suspended in water were investigated with dynamic light scattering (DLS) using a Zetasizer Nano ZS from Malvern Instruments equipped with a He/Ne 633 nm laser. Care was taken that the DLS peak position and

width were the same after three consecutive runs of 15 scans each run for all the nanoparticles. Number distribution data is reported.

Magnetic characterization was performed with a superconductive quantum interference device (SQUID) Quantum Design MPMS5XL magnetometer working in the temperature range 5–400 K and in magnetic field range 0–5 T. Zero field cooled (ZFC) and field cooled (FC) experiments were carried out by measuring the static magnetization at H_{DC} field of 50 Oe (4 kA m^{-1}) as the temperature was swept at a rate of 2 K/min from 5 to 300 - 400 K in samples cooled in absence of applied field, M_{ZFC} , and in samples cooled in H_{DC} field, M_{FC} . Isothermal specific magnetization, M , loops under applied magnetic field, H , at various temperatures between 5 and 300 K with maximum H of 5 T were performed in ZFC samples. a.c. susceptibility in the frequency range between 11 and 1000 Hz, were obtained with SQUID magnetometer and to enlarge a.c. measurements frequency range a.c. susceptibility option of Quantum Design PPMS 9T having a measuring range up to 10 kHz was also used. To avoid nonlinear magnetization effects a low enough field amplitude $H_{a.c.} = 5 \text{ Oe}$ (0.4 kA m^{-1}) was choose. Data were acquired at various frequencies ($f = \omega/2\pi$) ranging from 11 to 9999 Hz. The temperature range 5–300 K was well below the ordering temperature (873 K, 858 K) of the magnetic phase (maghemite, magnetite). Therefore changes in saturation magnetization M_s are rather small, and so the temperature dependence of M_s is neglected for a.c. susceptibility data analysis.

The samples were prepared using a gelatin capsules filled with compacted cotton impregnated with 50 μL of aqueous nanoparticles suspension giving a mass of around 1 mg of magnetic material, or just encapsulating the colloidal suspension into a heat shrinkable tube to prevent sample evaporation and spills. The specific magnetization values are reported per mass of iron.

Magnetocalorimetric experiments under radiofrequency fields for determining SAR were conducted by exposing 0.5 mL of the aqueous suspensions, held in a clear glass Dewar, to a field of frequencies of 163, 171, 190, 230 and 260 kHz and amplitudes from 16 to 52 kA m⁻¹. Field generator consists of a resonant RLC circuit Hüttinger (2.5/300) holding water refrigerated 6 turns coil of 2.5 cm diameter. Temperature was sensed during the experiment with an optical fibre sensor placed in the centre of the sample. The sensor was connected to a calibrated signal conditioner (Neoptix) of an accuracy of ± 0.1 °C. RF field application was interrupted to keep colloid temperature below 30 °C in order to minimize solvent evaporation and prevent its destabilization. Measurements were done by triplicate; reported values are average and s.d.

The SAR values were calculated from the initial slope $\partial T / \partial t$ of experimental heating

curves as $SAR = \frac{C}{[x]} \frac{\partial T}{\partial t}$ where C is the volumetric heat capacity of the solvent (4.18 J

K⁻¹cm⁻³). SAR is reported here, as W per gram of Fe. Heating curves are straight lines as commonly observed^{46,47}.

3. Specific absorption rate defining parameters

The specific heat released by a single domain MNP at a given field frequency f and amplitude H_0 depends on the magnetic relaxation mechanism achieved by the MNPs.

Within a characteristic time the magnetic moment switches from one direction to the opposite i.e. the magnetization reverses in coherent way due to Néel or Brown processes.

Brown relaxation times depend on medium viscosity, η , and hydrodynamic volume, V_H ,

as $\tau_B = \frac{3\eta V_H}{k_B T}$. The Néel relaxation time for uniaxial anisotropy depends on the energy

barrier, U , of a double-well potential and on the inverse attempt frequency

$\tau_0 \sim 10^{-13}$ - 10^{-10} s⁵⁵ as $\tau_N = \tau_0 \exp(U/k_B T)$. Extended expression to include field amplitude dependence is $\tau_{N,h} = \tau_0 \exp(U(1-h)^2/k_B T)$ where $h=H_0/H_k$, being H_k the anisotropy field⁵⁶. The dynamic of the particle's dipole moment is governed by the effective relaxation time, τ , given by $\tau^{-1} = \tau_N^{-1} + \tau_B^{-1}$. For independent relaxation modes⁵⁷ the faster occurs. Néel mechanism is inhibited ($\tau_N \gg \tau_B$) when the particles are large and/or have large magnetic anisotropy. Brown relaxation is inhibited ($\tau_N \ll \tau_B$) when the particles display large hydrodynamic volume and also hindered when the particles get fixed to cell membranes in the case by specific targeting⁵⁸.

The dissipation caused by these switching processes gives rise to a complex magnetic susceptibility. The imaginary part of the susceptibility, $\chi''(f)$, is proportional to the component of the magnetization that is induced out of phase with the excitation wave. This component is directly proportional to the specific rate of energy dissipation¹¹, known as SAR (specific absorption rate) parameter which is given within the lineal response approximation⁵⁹ and Stoner-Wohlfarth (SW) theory⁶⁰ by:

$$SAR = \mu_0 \pi f H_0^2 \int \chi''(f, \tau) g(\tau) d\tau \quad (1)$$

$$\text{With } \chi''(f, \tau) = \frac{2\pi f \tau}{1 + (2\pi f \tau)^2} \chi_0 \quad (2)$$

Where $g(\tau)$ is the relaxation time distribution due to nanoparticles size distribution, aggregation and dipolar interactions. At low field amplitude, χ_0 , can be approximated

$$\text{by the d.c. initial specific susceptibility}^{11} \text{ and modelled as } \chi_0 \cong \frac{\mu_0 \rho M_s^2 V}{3k_B T}.$$

By this way the mechanism executed by a MNP of a given chemical phase characterize by density ρ , at T, f and H_0 depends on nanoparticles physical properties such as shape, volume, V , (or size D) and its dispersion and magnetic properties such as, anisotropy and saturation magnetization, M_s , interparticle interaction (closely related to

concentration) and on its environment viscous and rheological properties. Eq. 1 indicates that the SAR of SD-MNPs suspensions increase with increasing field amplitude as H_0^2 , with increasing f in a more complex way through $f\chi''(f)$ factor (eq. 2), with increasing saturation magnetization as M_s^2 and with increasing V as $V\chi''(\tau(V))$ factor given by eq. 2. These dependences have been experimentally proved as it was briefly reviewed in the introduction^{16,43}.

The particles here studied dissipate by Néel relaxation mechanism. It will be shown in next section that τ_N is 6 orders of magnitude smaller than τ_B . Then, we will focus on the analysis of τ_N for complex colloids. For non-interacting particles of uniaxial anisotropy, U is related to MNP volume V as $K_{eff}V$, where K_{eff} is the effective anisotropy constant. Interparticle dipolar interaction increases relaxation time and has been modelled by adding a term to the energy barrier as $U=K_{eff}V+E_{int}$, where E_{int} represents mean field derived dipolar interparticle interaction energy or alternatively by decreasing thermal energy. The latter is known as Vogel-Fulcher correction and is a well-known approximation to account for weakly interacting nanoparticles⁶¹. It is clearly seen that the linear relation between U and V does not hold anymore for dipolar interacting nanoparticles simply recalling that dipolar interaction among two particles is proportional to the square root of the particle magnetic moment μ^2 ($M_s = \mu/V$). Also, K_{eff} contains crystallographic, shape and surface contributions, then at the nanoscale is highly dependent on nanoparticle size¹⁶.

4. Results and Discussion

As mentioned, we selected as model systems five stable colloidal aqueous suspensions to be studied on the basis of their distinctive M_{ZFC} and M_{FC} temperature behavior shown in figure 1 (right), with the aim of analysing activation energy, anisotropy and the

applicability of eq.1 to semi-empirically predict their SAR magnitude from the knowledge of their physical properties. These colloids consist of SD-IONPs of uniaxial anisotropy axes distributed in random directions. The mean MNP sizes cover a range from 5 to 14 nm, and they differ among them in nanoparticle size dispersity and structuring according to TEM images shown in figure 1 (left). The Cit/MNP-6 (mean size 6 nm) and Cit/MNP-8 (mean size 8 nm) particles are highly monodisperse and display somehow faceted faces. The CS/MNP-10 colloid consists of CS particles (~49 nm size) containing aggregates of 10 nm size MNPs densely packed. The distance between particles is close to contact distance, thus dipolar interactions are strong. On the other hand, CS/MNP-5 colloid consists of CS particles (~ 53 nm) containing well-spaced 5 nm size MNPs (almost no dipolar interactions are expected)⁴⁷. The U/MNP-14 displays the larger polydispersity and high degree of aggregation⁵². ED was carried out in all of the studied samples. ED images display well-defined diffraction rings that could be indexed to the cubic spinel structure (JCPDS #19-629) as it is exemplified in figure S1 of supplementary Information file (SI)). Also a XRD pattern and its refinement is shown in figure S1-c of SI file. Main structural data, mean size D and standard deviations (used here as a measurement of polydispersity degree) were derived from the fit of Gaussian distributions to size histograms built from TEM images (see table 1 and figure S1 of SI file).

Regarding M_{ZFC} and M_{FC} temperature behaviour, the Cit/MNP-6 nanoparticle assembly displays a well define narrow peak with a maximum at 38 K, above irreversible temperature T_i both curves coincide indicating superparamagnetic behaviour, and this region is well fitted by a Curie law function. The M_{ZFC} of CS/MNP-5 nanoparticle assembly peaks at 66 K, at a larger temperature than for Cit/MNP-6 although its size is smaller than Cit/MNP-6, due to larger size dispersity (see table 1). The Cit/MNP-8

nanoparticle assembly shows a somehow broader peak with a maximum at 111 K, CS/MNP-10 at 193 K, and U/MNP-14 well above room temperature. $M_{ZFC}(T)$ behaviour above T_i , departs from Curie law for all of these samples except for Cit/MNP-6. In Figure 1 samples are ordered with increasing blocking temperature, which also means increasing SAR magnitude, from top to bottom. The ZFC-FC magnetization curves besides reflecting structural features, mainly distinguish isolated particles from interactive particles behaviours. For example, FC curves (see Figure 1) reach a plateau in contrast to the increasing behaviour expected for random non-interacting particle system, pointing out a strong interaction between particles, more noticeable for CS/MNP-10 and U/MNP-14 samples. Interparticle interaction is detected by the shift of blocking temperature to higher values⁶². In complex colloids, this shift is also altered by features arising from polydispersity.

To get a better understanding on the influence of dipolar interaction, size dispersity and aggregation on the magnetization thermally activated behaviour; simulations of the M_{ZFC} were carried out following Tournus and Bonet model⁶³:

$$M_{ZFC} = \int_0^\infty \left(\frac{\mu_0 \mu(r)^2 H}{3K_{eff} V(r)} e^{-\nu \delta t} + \frac{\mu_0 \mu(r)^2 H}{3k_B T} (1 - e^{-\nu \delta t}) \right) g(r) dr \quad (3)$$

where, $\mu(r)$ is the magnetic moment of a nanoparticle of radius r , $\nu = 1/\tau$ being

$\tau = \tau_0 \exp \left[\frac{K_{eff} V(r)}{k_B (T - T_0)} \right]$ the Néel relaxation time including Vogel-Fulcher correction

T_0 , which will be retrieved below from a.c. data analysis, $\delta t = \frac{k_B (T - T_0)}{u K_{eff} V(r)}$ being u the

heating rate, and $g(r)$ the radii distribution derived from TEM (parameter listed in table 1) by fitting the histograms.

In figure 1 simulations carried out considering only size dispersity (null T_0) are shown as red lines and those considering both size dispersity and dipolar interactions (T_0 values

listed Table 2) are shown as blue lines. In the simulation at $T = T_0$ relaxation time is ∞ and all of the particles are blocked. The simulations take into account the effects of size dispersity and dipolar interaction but somehow disregard the effect of aggregation. The latter has been only considered through dipolar interactions within Vogel-Fulcher correction, which is a good approximation for weakly interacting nanoparticles. Clearly, interactions among particles inside an aggregate are expected to be strong. The simulations verify the fact that structuring, size dispersity and dipolar interactions play relevant role in the switching behaviour and then in the nanoparticles dissipation properties for MH.

From this data a distribution of activation energies $f(U)$ was obtained⁶⁴ as

$$\frac{\partial(M_{FC} - M_{ZFC})}{\partial T} \propto f(T_B) = \frac{f(U)}{k_B \ln(\tau_m / \tau_0)}, \text{ valid when } H_{DC} \text{ (4 kA m}^{-1}\text{) is smaller than}$$

anisotropy field H_K . The H_K magnitudes derived from 5 K magnetic loop (4000, 3197, 2798, 1040, 754 kA m⁻¹ for samples listed in table 1 from top to bottom) satisfy this condition. Results are shown in figure 2. Both, data and simulations verify the facts that blocking temperature increases with MNP size, and its value shifts to higher values with increasing size dispersity and interaction strength.

It can also be pointed out that ZFC/FC curves reflect magnetic anisotropic and dipolar interactions rather than Zeeman interaction because measurements are recorded at a low d.c field.

The precedent discussion proved that the idea of deriving K_{eff} from the blocking temperature $T_b = -U / (k_B \ln(\tau_0 / \tau_m))$ using $\tau_m = 100$ s and $U = K_{eff}V + E_{int}$ and $V = \langle V \rangle$ derived from TEM may result in not enough accurate K_{eff} value and fail to reproduce SAR values. The studied colloids display three not negligible characteristics: polydispersity, aggregation and dipolar interaction. Even Cit/MNP-6 and Cit/MNP-8

display size polydispersity and small aggregates as shown with cryo-TEM measurement (see figure 4). A colloid of nearly non-interacting MNPs can be obtained lowering concentration by dilution, but diluted colloids are far-away from the *in vivo* scenario¹² and even from the *in vitro* experiments where the MNPs are located in endosomes⁶⁵. Also for low concentration a larger volume would have to be injected to achieve the therapeutic temperature, overcoming tumour capacity and the minimum non-toxic dosage. Cytotoxicity depends on size, shape, charge, surface area, and aggregation of IONPs. Generally, it is found low or no cytotoxicity associated with the kind of IONPs here studied for exposure levels lower than 100 $\mu\text{g/mL}$ ⁶⁶. The concentrations here used, listed in table 1, are in the same order of magnitude of those used for *in vivo* experiments with mice tumour models⁶⁷. Also, there is usually not enough knowledge neither about the proportion of these three effects, nor the correlation among them, nor on how relaxation time is modified by them. Then, as a simple solution, we have derived the mean activation energy $\langle U \rangle$, which includes modifications of the energy barrier coming from the three mentioned effect. Values of $\langle U \rangle$ were consistently derived from independent measurements of a.c. susceptibility, coercive field, H_c , temperature dependence in the blocked range, as follows from d.c. hysteresis loops, ZFC/FC protocols and magnetocalorimetric measurements under RF fields. The $\langle U \rangle$ values found in this work are consistent with energy barrier values reported in literature for similar size iron oxide nanoparticles^{20,28,52, 68, 69} as shown in figure S2 in SI. Qualitative shape of activation energy distribution derived from ZFC/FC magnetization measurements are shown in figure 2. For all of the analysis τ_0 was fixed at 10^{-10} s. This attempt time value was chosen from the detail analysis of Dormann et al.⁶¹ who demonstrated, using a wide experimental measuring time range going from 10^{-8} to

10^{-1} s, that for interacting nanoparticles the dependence of $\log(\tau)$ against $(1/T_b)$ departs from Néel-Arrhenius law and asymptotically goes to $\tau_0=10^{-10}$ s.

Table 1. Synthesis conditions and colloids and nanoparticles properties. $[x]$ is the colloid concentration expressed as mg of iron per mL of water, D and $s.d$ are the mean MNP size and standard deviation determined from TEM histograms, D_H and $s.d_H$ are the hydrodynamic size and standard deviation of number distribution function derived from DLS measurements, μ and M_s are the mean nanoparticle magnetic moment and the saturation magnetization derived from the fit of d.c. magnetic loops measured at 300 K (see Figure S3 of SI file) and SAR is the specific absorption rate measured in the colloidal suspensions at a field frequency of 260 kHz and field amplitude of 52 kA m⁻¹. Co-pre stands for co-precipitation and TD-MW for thermal decomposition assisted with microwaves.

Sample	Synthesis protocol	$[x]$ (mg _{Fe} /mL)	D (nm)	$s.d$ (nm)	D_H (nm)	$s.d_H$ (nm)	μ (μ_B)	M_s (Am ² /kg _{Fe})	SAR (W/g _{Fe})
CS/MNP-5	Co-pre	1.2±0.1	4.8	2.1	134.6	7.7	4009±8	73.2±3.0	11±4
Cit/MNP-6	TD-MW	9.5±0.2	5.6	0.8	52.2	26.0	1763±2	57.5±2.9	9±1
Cit/MNP-8	TD-MW	14.7±0.3	8.0	2.0	17.2	4.8	7146±17	71.9±2.9	7±1
CS/MNP-10	Co-pre	2.3±0.1	9.7	4.5	56.9	7.7	8053±36	63.4±2.6	114±1
U/MNP-14	Co-pre	6.0±0.1	13.6	5.3	1500	500	13480±256	90.0±3.6	352±6

A.C. susceptibility measurements exhibited the typical expected behaviour for SD-MNP; **Error! Marcador no definido.** (Figure S4 of SI file). A well-defined maximum appears in the out-of-phase $\chi''(T)$ susceptibility at T_b . The peak positions shift with increasing frequency to higher values. Also $\chi''(T)$ peak becomes broader, and shifts towards higher temperatures for increasing size dispersity, aggregation and interactions strength. Then, Vogel–Fulcher criterion⁷⁰ was used to take into account these changes and to quantify interparticle interaction as $\ln\left(\frac{1}{2\pi f}\right) = \frac{U}{T_b - T_0} + \ln(\tau_0)$ where f is the excitation field frequency and T_0 is a parameter that globally accounts for interparticle interactions. Results are shown in figure 3a and U and T_0 fitted values are listed in table 2.

The H_c of an assembly of randomly oriented single-domain MNP exhibiting thermally activated coherent magnetization reversal follows, according SW theory, the relation⁷¹

$$H_c(T) = 0.96 \frac{K_{eff}}{\mu_0 M_s} \left[1 - \left(\frac{T}{T_b} \right)^{1/2} \right] = 0.96 \frac{U}{\mu_0 \mu} \left[1 - \left(\frac{k_B T \ln(\tau_m/\tau_0)}{U + k_B T_0 \ln(\tau_m/\tau_0)} \right)^{1/2} \right] \quad (4)$$

where in the right part of eq. 4 Vogel-Fulcher approximation for the relaxation time is included.

Figure 3b depicts the dependence of H_c against $(T/T_b)^{1/2}$. The larger the blocking temperature the smaller the slope of $H_c(T)$, and the larger the SAR. Data was fitted using μ and U as fitting parameters (see table 2) instead of K_{eff} and T_b as it is often found in the literature. The so-derived U values are in good agreement with those obtained from $\chi''(T)$ analysis. The fitted μ values are listed as μ_{Hc} in table 2 and are larger than μ of a SD-MNP (listed in table 1) reflecting aggregation. The ratio values $\frac{\mu_{Hc}}{\mu} = n_p$ are listed in table 2.

Aggregation can also be inferred from DLS, hydrodynamic sizes are listed in table 1. The colloids CS/MNP-5 and CS/MNP-10 are composed of polymeric particles holding well-spaced MNPs or its aggregates as can be seen by TEM as was previously shown with SAXS⁴⁷. For U/MNP-14 colloid, prepared with uncoated MNPs, aggregation happens at many length scales, as it is deduced from the large D_H value and also seen at TEM images. On the other hand, aggregation is not so clear in TEM images of Cit/MNP-6 and Cit/MNP-8 nanoparticles. Then, cryo-TEM was used to verify the presence of aggregates in these colloids. When the particles are prepared for cryo-TEM the cooling is so fast that the solvent freezes but the particle positions remain unchanged. In the images shown in figure 4, single particles and aggregates of only few particles can be observed. Chain-like arrangements appear consistent with dipole-dipole interactions minimum energy configuration (head-tail). The frequency n/N of number of aggregates n containing N_p particles, being N the total number of aggregates was derived from the images and is shown in the inset of figure 4. A large fraction of particles are composing small aggregates, 85 % for Cit/MNP-6 and 75 % for Cit/MNP-8. The previous analysis has shown that real colloids useful for biomedical applications, in

more or less degree, always displays size dispersity, aggregation and not neglectable interaction among particles, and this facts happens in both, colloids designed to display isolated particles and those designed to contain multicores.

The particles here studied dissipate by Néel relaxation mechanism, consistently Brown relaxation times estimated using water viscosity $\eta=0.7978 \times 10^{-3} \text{Pa}\cdot\text{s}$ and hydrodynamic sizes listed in table 1, results in relaxation times much larger than τ_N listed in table 2.

Next, we analyse the heating curves measured while the colloids were exposed to an excitation field of 260 kHz and 52 kA m^{-1} (raw data is shown in Figure S5 of SI file).

From SAR data combined with physical properties listed in table 1 we have extracted a mean $\langle \tau_{N,h} \rangle$ so that values obtained with equation 1 reproduce the experimental SAR values at the applied field condition. For this analysis we used Néel relaxation time as $\tau_{N,h}$, with h calculated using anisotropy field derived from 5 K magnetization curves.

By this way, it was possible to retrieve from the relaxation time (SAR measurements) a mean activation energy (listed in table 2 as U_{sar}). It can be seen that there is a good agreement between U values independently derived. Notice that low frequency a.c. measurement and d.c. magnetometry were carried out in frozen samples then the switching corresponds to Néel mechanisms. The good agreement between these U values with those derived from magnetocalorimetric measurements in the colloids confirms that Brown mechanism is inhibited in our colloids. Large differences appear for Cit/MNP-6.

We selected Cit/MNP-6 colloid, due to the large disagreement between different U measurements, and CS/MNP-10 colloid, due to higher SAR magnitude at our larger available f and H_0 condition, to examine frequency and field amplitude dependence. To this end, heating curves were recorded at various field amplitudes at a fixed frequency (see figure 5a) and at various field frequencies holding constant field amplitude (see

figure 5b). The SAR linearly increases with H_0^2 and with f as predicted with eq.1, as expected within linear response theory. Then, the so-derived relaxation time was used to extrapolate, using eq.1, the SAR to other frequencies and field amplitudes (red lines in figures 5a and 5b). It can be seen that the extrapolated values provide a good approximation to SAR values measured in these ranges of frequencies and amplitudes. Importantly, we have shown that the most significant physical property to be determined for predicting the heating efficiency of a given colloid is the distribution of activation energy or energy barrier. The latter contains contributions from anisotropy, dipolar interaction strength among particles and aggregation. As these features often appear in an uncontrolled manner, the specific proportion of the contribution of each property is disregarded, but the so-derived global mean activation energy includes all the mentioned contributions. We hither to conclude that the physical properties of a colloidal dispersion that must be determine to securely predict its heating efficiency at any pre-set applied field using the analytical expression (Eq.1) are mean activation energy, nanoparticle saturation magnetization and MNPs volume distribution. We believe that our finding may assist the medical decision serving at least as a guide for a better choice on optimal nanoparticle dosage, or at fixed dosage, better selection of clinical conditions. Overall, clinical settings, f and H_0 , jointly with MNP heating efficiency determine the dosage. In a first view, heating efficiency at a given field is determined by K , V , and M_s . However, concentration and aggregation plays a crucial role modifying the energy barrier. SAR concentration dependence is non-monotonous^{31,39}, due to the long range nature of dipolar interaction and aggregation may decrease heating efficiency when the magnetic moments are randomly oriented inside the aggregates^{30,31,32,33}, but the formation of elongated chains may improve it^{27,34}. Also aggregates compactness plays a role. In loose aggregates SAR decrease remained

moderate, being these decrease much larger for more compact packing³². These results stress the fact that magnetic hyperthermia prediction is a quite complex problem and the used of just K , V , and M_s is not enough for determining nanoparticles heating efficiency. Our solution differs from other previous proposed approaches by characterizing the material type with $\langle U \rangle$, $\langle V \rangle$ and M_s , where U includes other effects besides anisotropy terms (KV). A different promising strategy has been proposed by Ruggiero *et al.*¹⁴. The authors analysed oleate-covered iron oxide nanoparticles incorporated into poly(lactic-co-glycolic acid) particles and showed that ^1H nuclear magnetic relaxation dispersion profiles (as measured at very low magnetic fields, 0.01 MHz) can be correlated with the SAR of the system when exposed to an alternating magnetic field of 177 kHz y 18 kA m^{-1} .

The complexity of magnetic hyperthermia prediction increases when going to *in vitro* experiments where MNPs aggregates inside endosomes, where the number of filled endosome and their sizes vary from cell to cell, and the compactness of the MNPs inside the endosomes depends on the type of cell and on IONPs size distribution and surface charge. Less dense endosomes were observed for anionic magnetite nanoparticles comparing with the uncoated nanoparticle⁶⁵. Even a more complex scenario appears at *in vivo* experiments where after intratumoral infiltration irregular distribution patterns of the magnetic material occurs due to high interstitial pressures at the tumour area¹⁵. Although good results have been obtained pre clinically with animals the control of intratumoral distribution of the MNPs is an unsolved problem. It is clear that heating efficiency changes when going from the suspension to cell cultures or to tumours. Nevertheless, finding a way to predict SAR at various field conditions is the hurdles to be solved. Such knowledge together with controlled tumour distribution patterns will be useful to predict the heat distribution in the tumour.

Table 2. Activation energy and specific absorption rate. U_{Hc} , U_{AC} and U_{sar} are the mean activation energy values derived from coercive field temperature dependence, from a.c. susceptibility data analysis and from magnetocalorimetric measurements carried out at 260 kHz and 52 kA m⁻¹, respectively. The μ_{Hc} is a mean magnetic moment derived from $H_c(T)$ fit, n_p is the ratio $\frac{\mu_{Hc}}{\mu}$, T_o is the Vogel-parameter and $\langle\tau_N\rangle$ the mean relaxation time derived from SAR data analysis and τ_B is the Brown relaxation time.

Sample	U_{Hc} (10 ⁻²⁰ J)	μ_{Hc} (μ_B)	n_p	U_{AC} (10 ⁻²⁰ J)	T_o (K)	$\langle\tau_N\rangle$ (10 ⁻⁹ s)	τ_B (ms)	U_{sar} (10 ⁻²⁰ J)
CS/MNP -5	1.24±0.0 8	32827±5137	8±1	1.37±0. 14	0.01±0.46	5.0±0.9	0.70±0.01	1.40±0.08
Cit/MNP -6	0.74±0.0 1	12642±364	7±1	0.52±0. 06	13.45±2.50	8.1±0.8	0.04±0.01	1.09±0.04
Cit/MNP -8	1.09±0.0 2	18973±656	3±1	1.10±0. 13	38.69±5.47	2.0±0.3	0.0015±0.0 003	1.30±0.06
CS/MNP -10	3.27±0.0 8	65961±2901	8±1	3.13±0. 48	47.43±23.52	4.6±0.1	0.06±0.02	1.6±0.01
U/MNP- 14	6.2±0.2	174917±9016	13± 1	-	-	344±4	1030±38	7.19±0.01

4. Conclusions

We have addressed the issue of predicting the heating efficiency of real biomedical colloids for magnetic hyperthermia therapy. Real magnetic colloids are very complex systems because they display size dispersity, aggregation and its concentration must be in the useful range, where dipolar interactions are relevant. Comparing activation energy distribution, which defines Néel relaxation times, determined in four independent experiments, we can safely conclude that by knowing the mean nanoparticle volume, its saturation magnetization and a representative mean activation energy, the specific absorption rates can be predicted at a given field condition. This knowledge may assist the medical decision on the optimal nanoparticle dosage considering tumour's volume and the desired temperature increase.

Author Contributions

The manuscript was written through contributions of all authors. All authors have given approval to the final version of the manuscript.

ACKNOWLEDGMENT

This research was funded by CONICET (PIP 0720) and UNLP-X11/680 grants of Argentina and also partially funded by the Spanish Ministry of Economy (MAT2015-64442-R and SEV-2015-0496 projects, co-funded with European Social Funds) and the Generalitat de Catalunya (2014SGR213). We thank V. Lassalle for providing multicore nanoparticles, E. de Sousa for synthesizing uncoated nanoparticle and D. Muraca TEM data acquisition at Brazilian Nanotechnology National Laboratory (LNNano), Centro Nacional de Pesquisa em Energia e Materiais (CNPEM), Brazil under the Project No. TEM-MS-C-14825.

ABBREVIATIONS

CA, citric acid; DLS, Dynamic Light Scattering; FC, Field Cooling; ICP-AES, Atomic Emission Spectroscopy with Induced Plasma Coupled; IONPs, iron oxide nanoparticles; MNPs, magnetic nanoparticles; RF, radio frequency; SAR, specific absorption rate; SD, single domain; SQUID, Superconducting Quantum Interference Device; TEM, Transmission Electron Microscopy; ZFC, Zero Field Cooling.

Figures and Captions

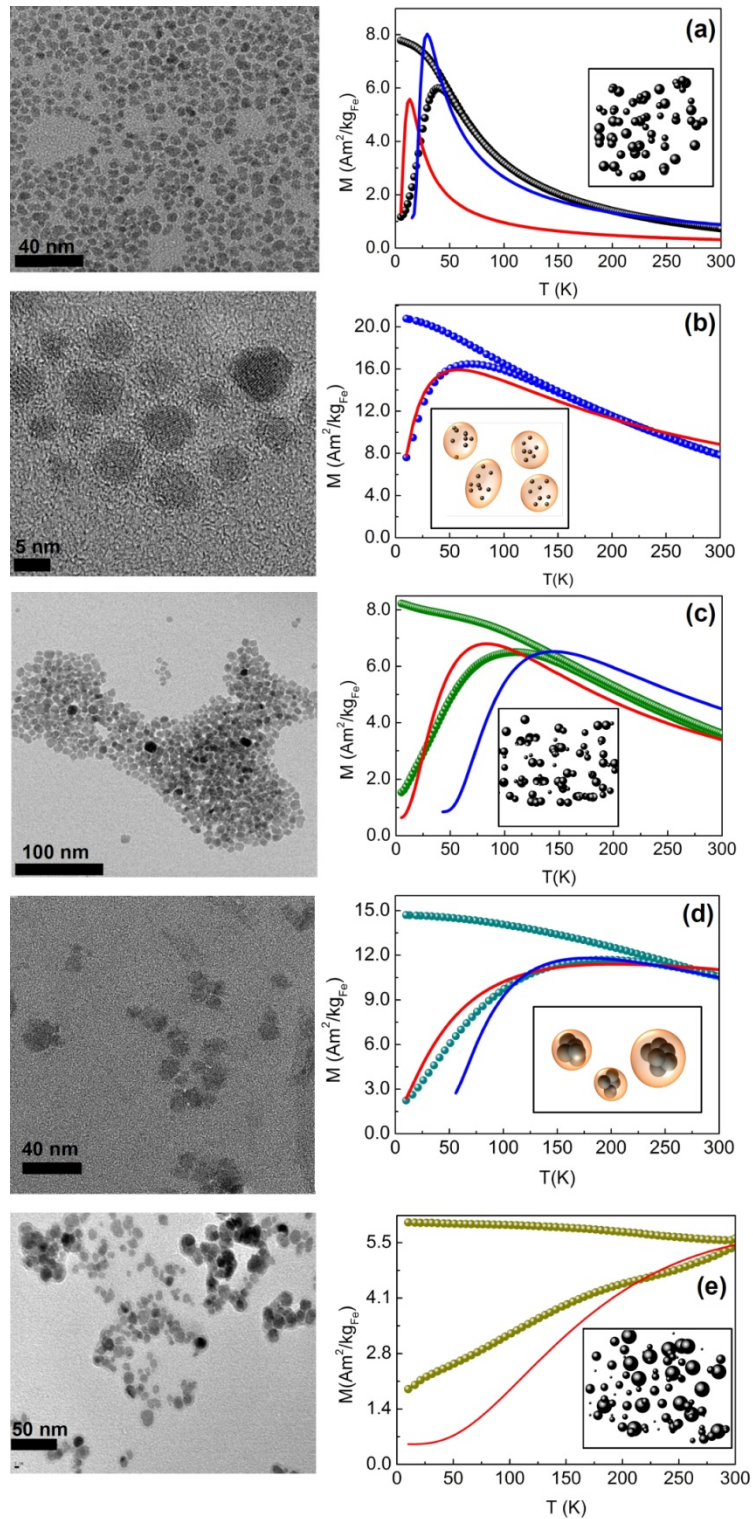


Figure 1: Representative TEM images, and magnetization behavior under ZFC/FC protocols for (a) Cit/MNP-6, (b) CS/MNP-5, (c) Cit/MNP-8, (d) CS/MNP-10 and (e) U/MNP-14. Continuous lines correspond to ZFC magnetization simulations using the Tournus and Bonet model⁶³ (eq. 3), red color considering size dispersity using distribution function derived from TEM images, and blue color considering both size dispersity and dipolar interaction using Vogel-Fulcher approximation. Cartoons on right plots schematize nanoparticles structuring.

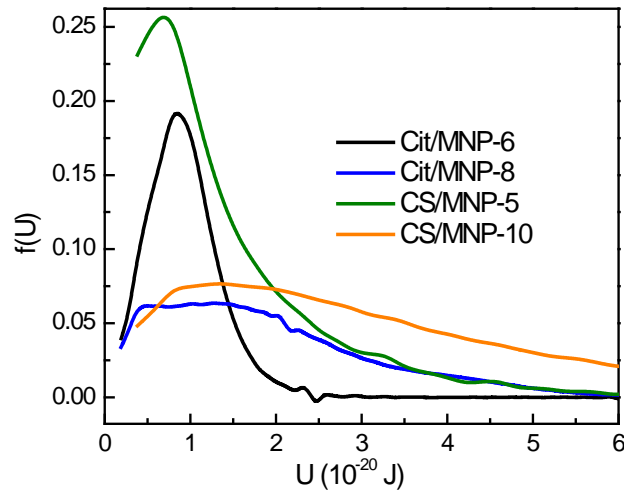


Figure 2: Activation energy distribution derived from ZFC/FC data.

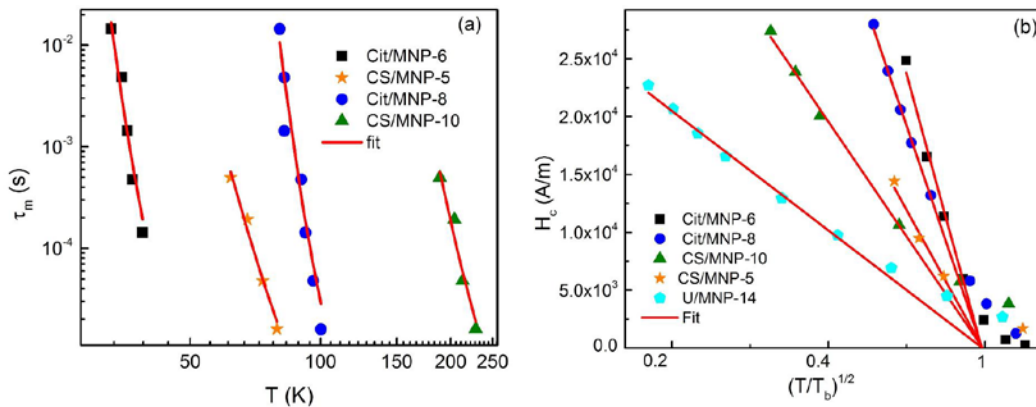


Figure 3: (a) Measuring time τ_m of a.c. susceptibility measurements vs. temperature T . Continuous lines represent the best fits obtained using the Vogel-Fulcher model. (b) Coercive field H_c temperature dependence derived from d.c. magnetization curves. T_b is the blocking temperature for squid measuring time $\tau_m = 100$ s and $\tau_o = 10^{-10}$ s. Continuous lines represent the best fits obtained using eq. 4. From these fits mean energy barrier U_{H_c} and mean magnetic moment μ_{H_c} are obtained.

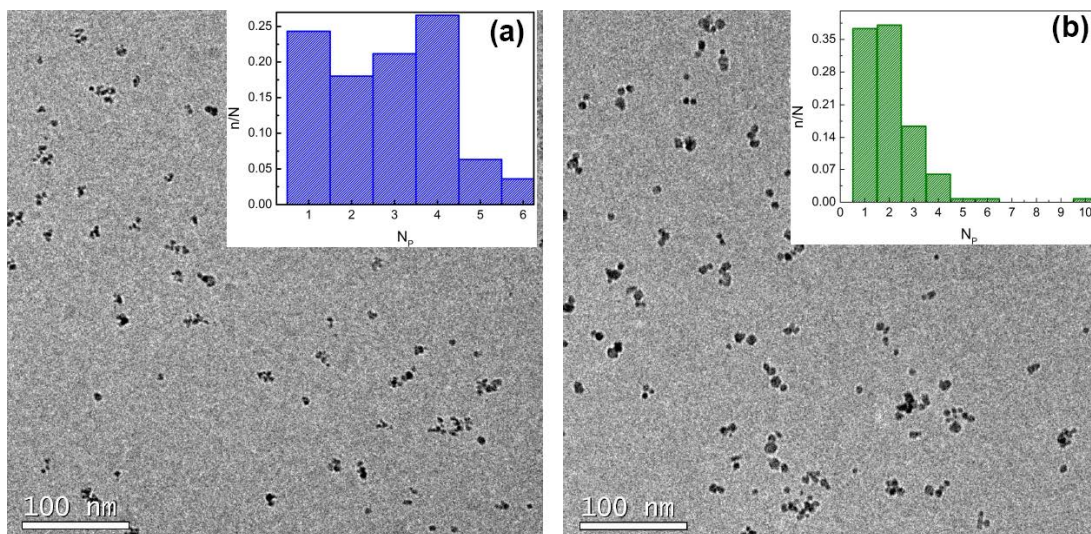


Figure 4. Cryo-TEM images of (a) Cit/MNP-6 and (b) Cit/MNP-8 samples. *Inset:* n/N is the frequency count of number of aggregates n containing N_p particles, being N the total number of aggregates.

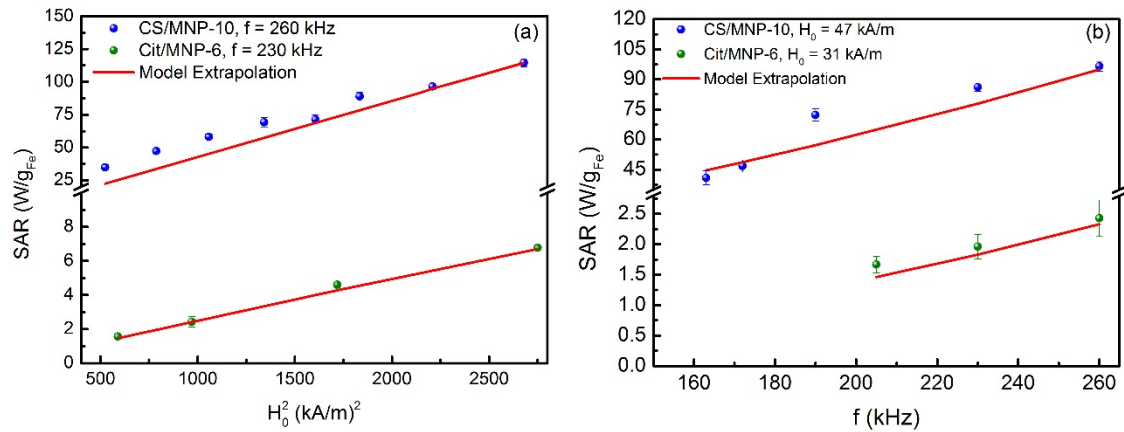


Figure 5: For sample CS/MNP-10 and Cit/MNP-6: (a) Specific absorption rate (SAR) vs. square field amplitude H_0 , (b) SAR vs. field frequency f . Continuous lines represent the extrapolation to different field conditions of Eq. 1 using the relaxation time retrieved from static and dynamic measurements.

References

- ¹K. Maier-Hauff, F. Ulrich, D. Nestler, H. Niehoff, P. Wust, B. Thiesen, H. Orawa, V. Budach, A. Jordan. *Journal of Neuro-oncology*, 2011, **103**, 317.
- ²Y. Ren, H. Zhang, B. Chen, J. Cheng, X. Cai, R. Liu, G. Xia, W. Wu, S. Wang, J. Ding, C. Gao, J. Wang, W. Bao, L. Wang, L. Tian, H. Song, X. Wang. *International Journal of Nanomedicine*, 2012, **7**, 2261.
- ³K. Sub Kim, J. Kim, J. Young Lee, S. Matsuda, S. Hideshima, Y. Mori, T. Osaka, K. Na. *Nanoscale*, 2016, **8**, 11625.
- ⁴A. Ruiz, P. C. Morais, R. B. de Azevedo, G. M. Lacava, A. Villanueva, M. del Puerto Morales. *J. Nanopart Res.*, 2016, **16**, 2589.
- ⁵M. Dan, Y. Bae, T.A. Pittman, R.A. Yokel. *Pharmaceutical Research*, 2014, **32** (5), 1615.
- ⁶Y. Zhai, H. Xie, H. Gu. *Int. J. Hyperthermia*, 2015, **25**(1), 65.
- ⁷I. Rabias, D. Tsitrouli, E. Karakosta. *Biomicrofluidics*, 2009, **4**(2), 024111
- ⁸A. Jordan, R. Scholz, K. Maier-Hauff, F.K. van Landeghem, N. Waldoefner, U. Teichgraber, J. Pinkernelle, H. Bruhn, F. Neumann, B. Thiesen, A. von Deimling, R. Felix. *J. Neurooncol.*, 2006, **78**(1), 7.
- ⁹P. Moroz, S. K. Jones, B. N. Gray. *Journal of Surgical Oncology*, 2001, **77**, 259.
- ¹⁰S. Luo, L.F. Wang, W.J. Ding, H. Wang, J.M. Zhou, H.K. Jin, S.F. Su, O.A. Ouyang. *Cancer*, 2014, **2**(1), 2.
- ¹¹R.E. Rosensweig. *Journal of Magnetism and Magnetic Materials*, 2002, **252**, 370.
- ¹²A. Jordan, R. Scholz, P. Wust, H. Fähling, R. Felix. *Journal of Magnetism and Magnetic Materials*, 1999,

201, 413.

¹³ J. Grossman, S. E. McNeil, *Phys. Today*, 2012, **65**(8), 38.

¹⁴ M. R. Ruggiero, S. G. Crich, E. Sieni, P. Sgarbossa, M. Forzan, E. Cavallari, R. Stefania, F. Dughiero, S. Aime, *Nanotechnology*, 2016, **27**, 285104

¹⁵ I. Hilgher. *International Journal of Hyperthermia*, 2013, **29**(8), 828.

¹⁶ I. M. Obaidat, B. Issa, Y. Haik, *Nanomaterials*, 2015, **5**, 63.

¹⁷ P. de la Presa, Y. Luengo, M. Multigner, R. Costo, M.P. Morales, G. Rivero, A. Hernando. *The Journal of Physical Chemistry C*, 2012, **116**(48), 25602.

¹⁸ R. Hergt, S. Dutz, R. Müller, M. Zeisberger. *Journal Physics: Condensed Matter*, 2006, **18**, 2919.

¹⁹ S. Sun, H. Zeng, D. B. Robinson, S. Raoux, P. M. Rice, S. X. Wang, G. Li. *Journal of the American Chemical Society*, 2004, **126**, 273.

²⁰ G. Salas, C. Casado, F. J. Teran, R. Miranda, C. J. Serna, M. Puerto Morales. *Journal of Materials Chemistry*, 2012, **22**, 21065.

²¹ P. Hugounenq, M. Levy, D. Alloyeau, L. Lartigue, E. Dubois, V. Cabuil, C. Ricolleau, S. Roux, C. Wilhelm, F. Gazeau, R. Bazzi. *The Journal of Physical Chemistry C*, 2012, **116** (29), 15702.

²² J. P. Novoselova, A. P. Safronov, O. M. Samatov, I. V. Beketov, H. Khurshid, Z. Nemati, H. Srikanth, T. P. Denisova, R. Andrade, G. V. Kuryandskaya, *IEEE Transactions on Magnetics*, 2014 **50** (11), 4600504.

²³ L. Gonzalez-Moragas, SM Yu, N Murillo-Cremaes, A Laromaine, A Roig, *Chemical Engineering Journal*, **2015**, 281, 87.

²⁴ C. Blanco-Andujar, D.Ortega, P. Southern, Q.A. Pankhurst, N.T. Thanh, *Nanoscale*, 2015, **7**(5), 1768.

²⁵ E. Alphanbéry, *Frontiers in Bioengineering and Biotechnology*, 2014, **2**, 5.

²⁶ M. Marciello, V. Connord, S. Veintemillas-Verdaguer, M.A. Vergés, J. Carrey, M. Respaud, C. J. Serna, M. Puerto Morales, *Journal of Material Chemistry B*, 2013, **1**, 5995.

²⁷ C. Martinez-Boubeta, K. Simeonidis, A. Makridis, M. Angelakeris, O. Iglesias, P. Guardia, A. Cabot, Ll. Yedra, S. Estrade, F. Peiro, Z. Saghi, P. A. Midgley, I. Conde-Leboran, D. Serantes, D. Baldomir, *Scientific Reports*, 2013, **3**, 1652.

²⁸ R. Di Corato, A. Espinosa, L. Lartigue, M. Tharaud, S. Chat, T. Pellegrino, C. Ménager, F. Gazeau, C. Wilhelm, *Biomaterials*, 2014, **35**, 6400.

²⁹ J.H. Lee, J.T. Jang, J.S. Choi, S.H. Moon, S.H. Noh, J.G. Kim, J.G. Kim, I.S. Kim. K.I. Park, J. Cheon,

Nat. Nanotechnol., 2011,**6**, 418.

³⁰J. G. Ovejero, D. Cabrera, J. Carrey, T. Valdivielso, G. Salas, F. J. Teran, Phys. Chem. Chem. Phys., 2016,**18**, 10954.

³¹D. F. Coral, P. Mendoza Zélis, M. Marciello, M. del Puerto Morales, A. Craievich, F. Sanchez, M. Fernández van Raap, Langmuir, 2016, **32** (5), 1201.

³²C. Guibert, V. Dupuis, V. Peyre, J. Fresnais, J. Phys. Chem. C, 2015, **119** (50), 28148.

³³M. E. Materia, P. Guardia, A. Sathya, M. Pernia Leal, R. Marotta, R. Di Corato, T. Pellegrino, Langmuir, 2015, **31** (2), 808.

³⁴D. Serantes, K. Simeonidis, M. Angelakeris, O. Chubykalo-Fesenko, M. Marciello, M. del Puerto Morales, D. Baldomir, C. Martinez-Boubeta, J. Phys. Chem. C, 2014, **118**, 5927.

³⁵M. Jeun, S. Bae, A. Tomitaka, Y. Takemura, K. Ho Park, S. Ha Paek, K. W. Chung, Applied Physics Letter, 2009, **95**, 082501.

³⁶A. Urtizberea, E. Natividad, A. Arizaga, M. Castro, A. Mediano, The Journal of Physical Chemistry C, 2010, **114** (11), 4916.

³⁷D. Serantes, D. Baldomir, C. Martinez-Boubeta, K. Simeonidis, M. Angelakeris, E. Natividad, M. Castro, A. Mediano, D. X. Chen, A. Sanchez, LI. Balcells, B. Martínez, Journal Applied Physics, 2010,**108**, 073918.

³⁸B. Mehdaoui, R. P. Tan, A. Meffre, J. Carrey, S. Lachaize, B. Chaudret, M. Respaud, Physical Review B. 2013,**87**, 174419.

³⁹I. Conde-Leboran, D. Baldomir, C. Martinez-Boubeta, O. Chubykalo-Fesenko, M. P. Morales, G. Salas, D. Cabrera, J. Camarero, F. Teran, D. Serantes, The Journal Physical Chemistry C, 2015, **119** (27), 15698.

⁴⁰G. T. Landi, Physical Review B, 2014, **89**, 014403.

⁴¹G. T. Landi, Journal Applied Physics, 2013, **113**, 163908.

⁴²C. Haase, U. Nowak, Physical Review B, 2012, **85**, 045435.

⁴³E. C. Abenojar, S. Wickramasinghe, J. Bas-Concepcion, A. C. S. Samia, Progress in Natural Science: Materials International 2016, **26**, 440.

⁴⁴G. Salas, J. Camarero, D. Cabrera, H. Takacs, M. Varela, R. Ludwig, H. Dähring, I. Hilger, R. Miranda, M. del Puerto Morales, F. J. Teran, The Journal Physical Chemistry C, 2014, **118** (34), 19985.

⁴⁵D. Kechrakos and K. N. Trohidou, Applied Physics Letter, 2002, **81**, 4574.

⁴⁶P. Mendoza Zélis, G. A. Pasquevich, S. J. Stewart, M. B. Fernández van Raap, J. Apesteguy, I. J.

-
- Bruvera, C. Laborde, B. Pianciola, S. Jacobo, F. H. Sánchez, *Journal of Physics D: Applied Physics*, 2013, **46**, 125006.
- ⁴⁷D. F. Coral, P. Mendoza Zelis, M. E. de Sousa, D. Muraca, V. Lassalle, P. Nicolas, M. L. Ferreira, M. B. Fernández van Raap, *Journal Applied Physics*, 2014, **115**, 043907.
- ⁴⁸E. Lima Jr., T. E. Torres, L. M. Rossi, H. R. Rechenberg, T. S. Berquo, A. Ibarra, C. Marquina, M. R. Ibarra, G. F. Goya, *Journal of Nanoparticle Research*, 2013, **15**, 1654.
- ⁴⁹M. S. Carrião, A.F.Bakuzis, *Nanoscale*, 2016, **8**, 8363.
- ⁵⁰J. M. Orozco-Henao, D.F. Coral, D. Muraca, O. Moscoso-Londoño, P. Mendoza Zélis, M. B. Fernández van Raap, S. K. Sharma, K. R. Pirota, M. Knobel, *J. Phys. Chem. C*, 2016, **120** (23), 12796.
- ⁵¹P. Nicolás, M. Saleta, H. Troiani, R. Zysler, V. Lassalle, M. L. Ferreira, *Acta Biomaterialia*, 2013, **9**(1), 4754.
- ⁵²M. E. de Sousa, M. B. Fernández van Raap, P. C. Rivas, P. Mendoza Zélis, P. Girardin, G. Pasquevich, J. Alessandrini, D. Muraca, F. H. Sánchez, *The Journal of Physical Chemistry C*, 2013, **117** (10), 5436.
- ⁵³S. Yu, A. Laromaine, A. Roig, *Journal of Nanoparticle Research*, 2014, **16**, 2484.
- ⁵⁴O. Pascu, E. Carezza, M. Gich, S. Estradé, F. Peiró, G. Herranz, A. Roig, *Journal of Physical Chemistry C*, 2012, **116**(28), 15108.
- ⁵⁵J. L. Dormann, L. Bessais, D. Fiorani, *Journal of Physics C: Solid State Physics*, 1988, **21**, 2015.
- ⁵⁶J. Dieckhoff, D. Eberbeck, M. Schilling, F. Ludwig, *J. Appl. Phys.*, 2016, **119**, 043903.
- ⁵⁷M. I. Shliomis, V. I. Stepanov, *Advances in Chemical Physics: Relaxation Phenomena in Condensed Matter*, John Wiley & Sons, 1994.
- ⁵⁸F. Sonvico, S. Mornet, S. Vasseur, C. Dubernet, D. Jaillard, J. Degrouard, J. Hoebeke, E. Duguet, P. Colombo, P. Couvreur, *Bioconjugate Chem*, 2005, **16**, 1181.
- ⁵⁹J. Jensen and A. R. Mackintosh, *Rare Earth Magnetism: Structures and Excitations*, Oxford, 1991.
- ⁶⁰E. C. Stoner and E. P. Wohlfarth, *Philosophical Transactions of the Royal Society A*, 1948, **240**, 599.
- ⁶¹J. L. Dormann, D. Fiorani, E. Tronc, *Magnetic relaxation in fine particle systems: in Advances in Chemical Physics*, John Wiley & Sons, 2007.
- ⁶²J. M. Vargas, W. C. Nunes, L. M. Socolovsky, M. Knobel, and D. Zanchet, *Phys. Rev. B*, 2005, **72**, 184428.
- ⁶³F. Tournus, E. Bonet, *Journal of Magnetism and Magnetic Materials*, 2011, **323**, 1109.
- ⁶⁴F. Luis, J. M. Torres, L. M. García, J. Bartolomé, J. Stankiewicz, F. Petroff, F. Fetta, J.-L. Maurice, A.

Vaurés, Physical Review B, 2002, **65**, 094409.

⁶⁵M. Elisa de Sousa, A. Carrea, P. Mendoza Zéllis, D. Muraca, O. Mykhaylyk, Y. E. Sosa, R. G. Goya, F. H. Sánchez, R. A. Dewey, M.B. Fernández van Raap, J. Phys. Chem. C, 2016, **120** (13), 7339.

⁶⁶U. S. Patil, S. Adireddy, A. Jaiswal, S. Mandava, B. R. Lee, D. B. Chrisey, Int J Mol Sci. 2015, **16**(10), 24417.

⁶⁷S. Kossatz, R. Ludwig, H. Dähring, V. Ettelt, G. Rimkus, M. Marciello, G. Salas, V. Patel, F. J. Teran, I. Hilger, Pharmaceutical Research, 2014, **31**, 3274.

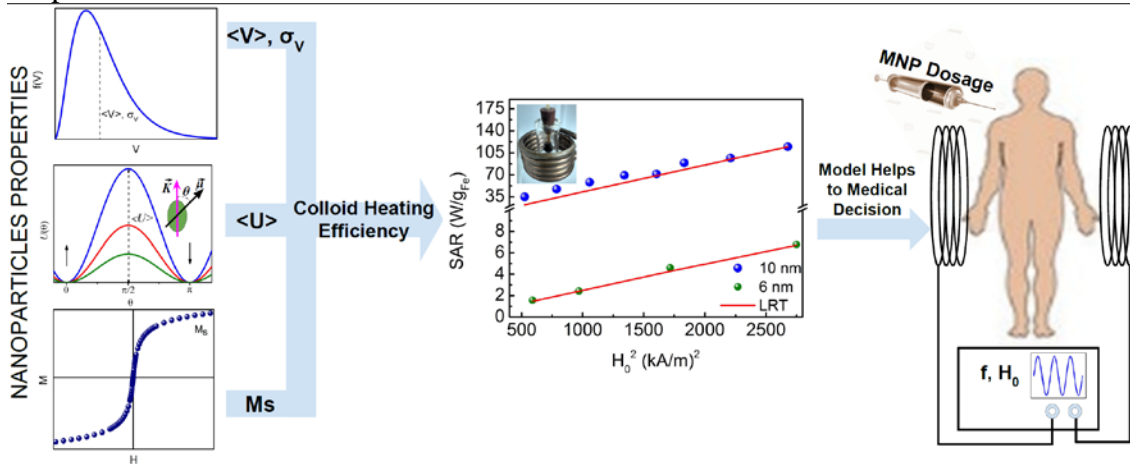
⁶⁸V. Dolgovskiy, V. Lebedev, S. Colombo, A. Weis, B. Michen, L. Ackermann-Hirschi, A. Petri-Fink, Journal of Magnetism and Magnetic Materials, 2015, **379**, 137.

⁶⁹G. Vallejo-Fernandez, O. Whear, A.G. Roca, S. Hussain, J. Timmis, V. Pattel, K.O'Grady, Journal of Physics D: Applied Physics, 2013, **46**, 312001.

⁷⁰J. L. Dormann, L. Spinu, E. Tronc, J. P. Jolivet, F. Lucari, F. D. D'Orazio, D. Fiorani, Journal of Magnetism and Magnetic Materials, 1998, **183**, 255.

⁷¹H. Pfeiffer, Physica Status solidi A, 1990, **119**, 295.

Graphical Abstract



Semi-empirical modeling of small nanoparticles heat dissipation helps the designing of medical decisions for clinical cancer magnetic hyperthermia.